The Cryosphere Discuss., 9, 495–539, 2015
www.the-cryosphere-discuss.net/9/495/2015/
doi:10.5194/tcd-9-495-2015

The Cryosphere Discussions
Open Access

Numerical simulation of extreme snow melt observed at the SIGMA-A site, northwest Greenland, during summer 2012

M. Niwano[1], T. Aoki[1], S. Matoba[2], S. Yamaguchi[3], T. Tanikawa[4], K. Kuchiki[1], and H. Motoyama[5]

[1]Meteorological Research Institute, Japan Meteorological Agency, Tsukuba, Japan
[2]Institute of Low Temperature Science, Hokkaido University, Sapporo, Japan
[3]Snow and Ice Research Center, National Research Institute for Earth Science and Disaster Prevention, Nagaoka, Japan
[4]Earth Observation Research Center, Japan Aerospace Exploration Agency, Tsukuba, Japan
[5]National Institute of Polar Research, Tachikawa, Japan

Received: 24 November 2014 – Accepted: 18 December 2014 – Published: 20 January 2015

Correspondence to: M. Niwano (mniwano@mri-jma.go.jp)

Published by Copernicus Publications on behalf of the European Geosciences Union.

Abstract

The surface energy balance (SEB) from 30 June to 14 July 2012 at site SIGMA (Snow Impurity and Glacial Microbe effects on abrupt warming in the Arctic)-A, (78°03′ N, 67°38′ W; 1490 m a.s.l.) on the northwest Greenland Ice Sheet (GrIS) was investigated by using in situ atmospheric and snow measurements, as well as numerical modeling with a one-dimensional, multi-layered, physical snowpack model called SMAP (Snow Metamorphism and Albedo Process). At SIGMA-A, remarkable near-surface snowmelt and continuous heavy rainfall (accumulated precipitation between 10 and 14 July was estimated to be 100 mm) were observed after 10 July 2012. Application of the SMAP model to the GrIS snowpack was evaluated based on the snow temperature profile, snow surface temperature, surface snow grain size, and shortwave albedo, all of which the model simulated reasonably well. However, comparison of the SMAP-calculated surface snow grain size with in situ measurements during the period when surface hoar with small grain size was observed on-site revealed that it was necessary to input air temperature, relative humidity, and wind speed data from two heights to simulate the latent heat flux into the snow surface and subsequent surface hoar formation. The calculated latent heat flux was always directed away from the surface if data from only one height were input to the SMAP model, even if the value for roughness length of momentum was perturbed between the possible maximum and minimum values in numerical sensitivity tests. This result highlights the need to use two-level atmospheric profiles to obtain realistic latent heat flux. Using such profiles, we calculated the SEB at SIGMA-A from 30 June to 14 July 2012. Radiation-related fluxes were obtained from in situ measurements, whereas other fluxes were calculated with the SMAP model. By examining the components of the SEB, we determined that low-level clouds accompanied by a significant temperature increase played an important role in the melt event observed at SIGMA-A. These conditions induced a remarkable surface heating via cloud radiative forcing in the polar region.

TCD
9, 495–539, 2015

1 Introduction

Snow and ice on the Greenland ice sheet (GrIS) experienced a record near-surface melt extent in summer 2012 (Nghiem et al., 2012; Tedesco et al., 2013; Hall et al., 2013; Hanna et al., 2014; Bennartz et al., 2013). The physical conditions of the atmosphere and the snow (as well as ice) surface during summer 2012 have been gradually clarified. The most notable feature of the event is that the extent of surface melt was the largest in the satellite era (March 2000 to the present). According to several studies that used satellite data (Nghiem et al., 2012; Tedesco et al., 2013; Hall et al., 2013), at least 95 % of the entire surface of the GrIS melted during the period 30 June to 14 July 2012. At present, it is hypothesized that a significant temperature increase over the GrIS may have been a major cause of the record near-surface melt event. Hall et al. (2013) examined the ice surface temperature (IST) of the GrIS derived from the Moderate-resolution Imaging Spectroradiometer (MODIS) and concluded that the 2012 summer was the warmest (IST: $-6.38 \pm 3.98\,^{\circ}\mathrm{C}$) in the MODIS record. Bennartz et al. (2013) have demonstrated that low-level clouds consisting of liquid-water droplets played a key part in the melt event by increasing near-surface temperature via radiative effects. Nghiem et al. (2012) pointed out the existence of an anomalous ridge of warm air that could be identified by a 500 hPa height anomaly, and they concluded that the ridge acted as a strong heat dome that became stagnant over the GrIS during the period. Hanna et al. (2014) concluded that the extreme melt was forced mainly by atmospheric conditions linked with changes in the summer North Atlantic Oscillation (NAO), Greenland Blocking Index (GBI), and polar jet stream. The combination of these conditions favored southerly warm air advection along the western coast. According to Fettweis et al. (2013), the frequency of occurrence of anticyclones centered over the GrIS at the surface and at 500 hPa has doubled since the end of the 1990s. They associated this increased frequency with an increase of negative phases of the NAO, which induce more frequent southerly warm air advection along the western Greenland coast and over the neighboring Canadian Arctic Archipelago.

TCD
9, 495–539, 2015

However, a temperature increase is unlikely to be the only cause of surface melt, because surface melt is physically controlled by the surface energy balance (SEB). The SEB is equal to the sum of the net shortwave radiant flux, net longwave radiant flux, sensible heat flux, latent heat flux, heat supply by rainfall, and subsurface conductive heat flux (Armstrong and Brun, 2008). In this study, these fluxes were defined to be positive when they were directed towards the snow surface, and a positive sum of these fluxes (net energy flux) induces surface melt. A temperature increase raises the net energy flux mainly by affecting the sensible heat flux, although other energy fluxes, especially net longwave radiant flux, can of course be affected by a temperature increase. Therefore, it is necessary to pay close attention to other fluxes in addition to the sensible heat flux when surface melt is investigated.

In the present study, our goal was to understand the record near-surface melt event that occurred over the GrIS in 2012 by investigating snow-atmosphere interactions from the standpoint of the SEB. For this purpose, we employed data obtained from in situ measurements made at a site named SIGMA (Snow Impurity and Glacial Microbe effects on abrupt warming in the Arctic)-A (Aoki et al., 2014a) in northwest Greenland during the 2012 summer intensive observation period (30 June to 14 July) (hereafter: IOP). During the latter half of the IOP, which coincided with the period of the record near-surface melt event reported by Nghiem et al. (2012), we observed remarkable melting of the near-surface snowpack and encountered continuous rainfall (Aoki et al., 2014b; Yamaguchi et al., 2014). In the process of calculating the SEB, radiation-related terms could be determined from in situ measurements (described in Sect. 2); however, the sensible heat flux, latent heat flux, and heat supply by rainfall, which were not measured directly at the SIGMA-A site, had to be calculated in some way. In this study, we therefore calculated these fluxes by using the physical snowpack model SMAP (Snow Metamorphism and Albedo Process), which was originally developed and evaluated against seasonal snowpack (Niwano et al., 2012, 2014). Because this study was the first attempt to apply the SMAP model in a polar region, we carried out a preliminary examination of various aspects of the capacity of the SMAP model. This model valida-

TCD
9, 495–539, 2015

tion study was expected to increase the reliability both of the SMAP model itself and of the Meteorological Research Institute Earth System Model version1 (MRI-ESM1) (Yukimoto et al., 2011), in which the SMAP model is used to calculate energy exchanges between the snow surface and atmosphere in the global cryosphere.

We begin part 2 of this paper by presenting an outline of our in situ measurements conducted at SIGMA-A during summer 2012. Then we describe the modification of the SMAP model that enabled its use to simulate polar conditions. We verified the accuracy of the model with respect to the snow temperature profile, snow surface temperature, surface optically equivalent snow grain radius, and shortwave albedo. Finally, we used the SMAP model to explore the SEB during the IOP at the SIGMA-A site by diagnosing the turbulent heat fluxes and heat supplied by rainfall.

2 Field measurements at the SIGMA-A site

In this section we report the in situ data acquired during the IOP at site SIGMA-A (78°03′ N, 67°38′ W, 1490 m a.s.l.) (Aoki et al., 2014a) in northwest Greenland (Fig. 1), and we report the observed meteorological and snow conditions. An automated weather station (AWS) was newly installed at site SIGMA-A on 29 July 2012 (Aoki et al., 2014a). This region of the northwestern GrIS is now being carefully monitored, because since around late 2005 the ice loss over southern portions of the GrIS has been spreading rapidly northward along the northwest coast (Khan et al., 2010). Dates and times throughout this paper are expressed in terms of the universal time clock (UTC); the difference between local time (LT) at site SIGMA-A and UTC is −2 h.

2.1 Meteorological observations

The AWS measured air temperature and relative humidity with a humidity and temperature probe (HMP155, Vaisala, Finland) protected from direct solar irradiance by a naturally aspirated, 14-plate Gill radiation shield (41005, Young, USA) at 3.0 and

TCD
9, 495–539, 2015

6.0 m above the snow surface on 29 June. According to van den Broeke et al. (2009), radiation errors in the unventilated air temperature measurement can be up to 3 °C under conditions of low wind speed and high insolation. However, no corrections were made to measured air temperature in the present study, because low wind speeds ($< 1.0\,m\,s^{-1}$) were rarely observed at SIGMA-A during IOP as noted later in this section. The AWS also measured wind speed and direction with a wind monitor (05103, Young, USA) at 3.0 and 6.0 m above the surface. The AWS was also equipped with a digital barometer (PTB210, Vaisala, Finland), and an ultrasonic distance sensor (SR50, Campbell, USA) for snow depth monitoring. We used a net radiometer (CNR4, Kipp & Zonen, Netherlands) to measure downward and upward shortwave (wavelength $\lambda = 0.305$–$2.8\,\mu m$) and longwave ($\lambda = 4.5$–$42\,\mu m$) radiant fluxes. Downward and upward near-infrared ($\lambda = 0.715$–$2.8\,\mu m$) radiant fluxes were observed by pyranometers (CMP6, Kipp & Zonen, Netherlands) with RG715 cut-off filter domes. Measured data were averaged every 1 min and stored in a data logger (CR1000, Campbell, USA). Aoki et al. (2014a) have provided a more detailed description of the AWS. In the present study, we used 5 min average values of AWS data, but to highlight important temporal evolution, the SEB data reported after Sect. 5 are 1 h averages.

In addition to the automatic measurements, we performed manual spectral albedo measurements using a field spectroradiometer (FieldSpec 3, Analytical Spectral Devices, Inc., USA) ($\lambda = 0.35$–$2.5\,\mu m$). The details of the measurement procedure were based on the method of Aoki et al. (2000). Use of the obtained spectral albedo in a GSAF (ground-based spectral radiometer system for albedo and flux; Kuchiki et al., 2009) channel with a λ of 1.23 µm allowed us to retrieve the surface optically equivalent snow grain radius (hereafter simply referred to as the "snow grain size" unless otherwise stated) with the GSAF algorithm developed by Kuchiki et al. (2009). In the latest version of this algorithm, the model of snow grain shape can be arbitrarily chosen to be a sphere, spheroid, or Voronoi aggregate. In this study we selected the Voronoi aggregate model developed by Ishimoto et al. (2012), because this choice led to the best agreement with in situ, manually measured surface snow grain size in

TCD
9, 495–539, 2015

the case of our data (see Sect. 2.2). We henceforth refer to this data as snow grain size retrieved by ground-based remote sensing (GRS). We used GRS data for model evaluation (Sect. 4.3).

Figure 2 presents time series of meteorological conditions measured with the AWS during the IOP. Until 9 July, air temperature at 3.0 m above the surface was already high and often exceeded 0 °C in the daytime. The time interval from 10 July until the end of the IOP coincided with the record near-surface melt event period reported by Nghiem et al. (2012); during that time air temperature increased slightly and remained above 0 °C continuously (Fig. 2a). The relative humidity recorded at 3.0 m above the surface was related to the high air temperature and tended to be high, the values sometimes approaching 100 % (Fig. 2a). At site SIGMA-A, low wind speeds ($< 1.0\,m\,s^{-1}$) were rarely observed at 3.0 m above the surface during the IOP (Fig. 2b). The gradual day-by-day rise of air temperature was accompanied by a strong southeast wind with a speed sometimes over $10\,m\,s^{-1}$. Radiation parameters (Fig. 2c) reflect sky conditions. For example, until 3 July and around 9 July, we observed clear-sky conditions on-site. During the clear-sky period, the downward shortwave and near-infrared radiant fluxes showed an obvious diurnal cycle, whereas the downward longwave radiant flux was almost constant. In contrast, cloudy-sky conditions (subjectively observed prevailing cloud types were Cumulus, Stratocumulus, and sometimes Stratus) on 3, 4, 6, 7, and 8 July and after 10 July were characterized by reduced downward shortwave and near-infrared radiant fluxes and increased downward longwave radiant flux. During such conditions, the near-infrared fraction of the downward shortwave radiant flux decreased to around 0.3, while it was around 0.5 under clear-sky conditions.

At the SIGMA-A site, no rainfall was observed on-site until 9 July. After 10 July, we encountered continuous rainfall till 14 July (Aoki et al., 2014b; Yamaguchi et al., 2014). Because precipitation is one of the critical parameters for a snowpack model that is used to calculate mass balance of a snowpack, the total amount of precipitation during 10–14 July was estimated on the basis of precipitation collected with a bucket during the period from 12 July, 20:00 UTC to 14 July, 11:00 UTC, and on the 3 hourly

TCD
9, 495–539, 2015

European Centre for Medium-Range Weather Forecasts (ECMWF) Interim reanalysis (ERA-Interim) data (Dee et al., 2011). At first, the precipitation that accumulated in the bucket from 12 July, 20:00 UTC to 14 July, 11:00 UTC and the 3 hourly ERA-Interim reanalysis data were compared. For this comparison, ERA-Interim 1 h accumulated precipitation was simply estimated to be one-third of the 3 hourly accumulated precipitation. The comparison indicated that the accumulated precipitation obtained from the ERA-Interim reanalysis data was lower by a factor of 1/4.9. The most prevailing reason for this discrepancy was not a misrepresentation of the true area of rainfall, but just underestimation by the ERA-Interim reanalysis (Fig. 3). Finally, the precipitation that accumulated between 10 and 14 July, 100 mm, was obtained by multiplying ERA-Interim reanalysis data by a factor of 4.9 (Fig. 2d). The procedure to input this information into the SMAP model is described in Sect. 3.3.

2.2 Snow pit measurements

Over the course of the IOP, we performed snow pit observations in the local morning (around 09:30 LT) to be able to characterize the snow physical profiles (Yamaguchi et al., 2014). We also collected near-surface snow samples to measure the mass concentrations of light-absorbing snow impurities such as black carbon (BC) and dust (Aoki et al., 2014b).

The near-surface layer of the snow was recognizable by quite a thick bottom ice layer. We focused on this near-surface layer in the snow pit observations, which were performed every day from 30 June to 13 July, except for 11 and 12 July, when there was heavy rain at the SIGMA-A site. The depth of the layer (above the ice layer) was 88 cm on 30 June. In this paper we refer to this target near-surface layer as the "NSL". Measured properties included profiles of snow grain shape, snow temperature (including bottom ice layer temperature), snow density, volumetric water content, and geometric snow grain size. In addition, the snow grain size of the top 10 cm was measured manually after 1 July. In this snow grain size measurement process, we followed the definition of "r_2" presented by Aoki et al. (2000, 2003, and 2007): one-half the branch

TCD
9, 495–539, 2015

width of dendrites or one-half the width of the narrower portion of broken crystals. Figure 4 shows the temporal evolution of the observed snow grain shape profile in the NSL at the SIGMA-A site from 30 June to 13 July 2012. On the whole, until 9 July this layer could be roughly divided into three parts: a bottom layer composed of depth hoar, a middle layer of rounded grains (sometimes including faceted crystals), and a top layer composed of melt forms, including an ice layer of variable thickness. After 10 July, a wet snow layer expanded from the top to the bottom as the air temperature increased slightly (Fig. 2a), and the rainfall event occurred (Fig. 2d). The measured snow temperature profile is presented in Sect. 4.1 and compared to the results simulated by the SMAP model. As for the other snow properties, we used only the data that we obtained on 30 June to specify the initial physical conditions of the snowpack at the SIGMA-A site for the SMAP model simulations. The procedure is briefly explained in Sect. 3.3.

Snow samples to measure the mass concentrations of snow impurities were collected from the top 2 cm and the 2–10 cm layer every other day from 30 June to 12 July (Aoki et al., 2014b). To obtain the mass concentrations of elemental carbon (EC), the samples were melted and filtered on-site, and the filters were weighed and assayed with a carbon analyzer (Lab OC-EC Aerosol Analyzer, Sunset Laboratory Inc., USA). In this study, we assumed, following Aoki et al. (2011), that EC was equivalent to BC. The dust concentrations were determined by subtracting total carbon concentrations from the total impurity concentrations, which were estimated from the difference between the dry weights of the filters before and after filtering (Aoki et al., 2003, 2007). The detailed analytical procedure is precisely described by Kuchiki et al. (2009) and Aoki et al. (2011, 2014b). Figure 5 shows the temporal changes in the mass concentrations of EC and dust in the near-surface snowpack at the SIGMA-A site during the IOP; the EC concentrations increased rapidly after 6 July. Aoki et al. (2014b) have discussed the reasons for this obvious increase, and they concluded that effects of sublimation/evaporation and snow melt amplification due to the low scavenging efficiency of meltwater played an important role.

TCD
9, 495–539, 2015

3 Numerical simulation with the SMAP model

3.1 SMAP model overview

The multilayered physical snowpack model SMAP calculates mass and energy balances of the snowpack by taking snow settlement, phase changes, water percolation, and snow metamorphism into account. The most distinguishing characteristic of the SMAP model is the fact that it incorporates the Physically Based Snow Albedo Model (PBSAM) developed by Aoki et al. (2011). PBSAM calculates snow albedo and the solar heating profile in the snowpack by explicitly considering effects of snow grain size and light-absorbing snow impurities such as BC and mineral dust. In default configuration, the SMAP model requires precipitation, air pressure, wind speed, air temperature, relative humidity, downward ultraviolet (UV)-visible and near-infrared radiant fluxes, the diffuse components of UV-visible and near-infrared radiant fluxes, downward longwave radiant flux, subsurface heat flux, and the mass concentrations of snow impurities (BC and dust) (Niwano et al., 2012). In the present study, the diffuse components of the UV-visible and near-infrared radiant fluxes were not available, as explained in Sect. 2.1. Under these circumstances, SMAP calculates these fluxes by using the scheme of Goudriaan (1977), together with internally diagnosed cloud fraction calculated from air temperature and simulated net longwave radiant fluxes at the snow surface. The procedure for obtaining cloud fraction is based on the approach of van den Broeke et al. (2004, 2006). Niwano et al. (2014) used data obtained during the winters of 2007–2009 at Sapporo to investigate the effectiveness of the process, and they demonstrated that the accuracy of the simulated snow depth and snow surface temperature were comparable in magnitude to the accuracy of the default configuration.

The main governing equation of the SMAP model is a one-dimensional energy balance equation that takes solar heating of the snowpack and melt-freeze cycles into account (Niwano et al., 2012). This equation is approximated and solved with the Crank–Nicolson finite difference implicit method. In this numerical solution, the SMAP model

TCD
9, 495–539, 2015

assumes each model snow layer to have a thickness d that is allowed to range between d_{min} and d_{max}. The values of d_{min} and d_{max} used in the present study are discussed in Sect. 3.3. Solar heating of the snowpack was calculated with a component of PBSAM. Input requirements for this component include internally calculated profiles of snow grain size and snow water equivalent (SWE), as well as the mass concentrations of snow impurities given externally from in situ measurements or host global or regional circulation models. Snow grain size was calculated by employing a model geometry that envisions two spherical ice particles connected by a neck (Lehning et al., 2002). By calculating the specific surface area (SSA) of snow per unit volume with the nonspherical model geometry, SMAP obtains snow grain size. Temporal evolution of snow grain size is governed by following three types of metamorphism regimes: equi-temperature metamorphism, temperature-gradient metamorphism, and wet snow metamorphism. The formulation of these metamorphism laws is based on results from the SNOWPACK model (Lehning et al., 2002). Furthermore, the SMAP model implicitly takes into account the effects of snow metamorphism under alternating temperature gradients (small rounded grains can be formed even when the temperature gradient is large if the sign of the temperature gradient changes with a 24-h cycle.) (Pinzer and Schneebeli, 2009) by forcing temperature gradient metamorphism, which generally induces rapid grain growth, not to occur in the top 20 cm of the each model layer.

Recently, the SMAP model was updated with respect to water movement in the snowpack, snow settlement, and turbulent heat exchanges under very stable conditions (Niwano et al., 2014). Water movement in the snowpack is now governed by the Richards equation (Richards, 1931), which takes into consideration Darcy's law; hydraulic diffusivity and hydraulic conductivity are calculated by the van Genuchten model (van Genuchten, 1980) adapted to snow (Shimizu, 1970; Hirashima et al., 2010; Yamaguchi et al., 2010, 2012). As for snow settlement, the updated version of the SMAP model calculates the viscosity coefficient of snow using the scheme presented by Vionnet et al. (2012), which was developed to improve the performance of the Crocus model (Brun et al., 1989, 1992; Vionnet et al., 2012; Carmagnola et al., 2014). To ensure min-

TCD
9, 495–539, 2015

imum turbulent heat exchanges under very stable conditions, we set an upper bound of 0.1 on the Richardson number.

3.2 Adaption of the SMAP model to the Greenland snowpack

In this section we discuss the adaptation of the model that enabled the SMAP model to be suitable for polar (especially Greenland) snowpack simulations. To simulate the temporal evolution of snow temperature accurately by solving the one-dimensional energy balance equation in the snowpack, the thermal conductivity of snow k_{eff} ($\mathrm{W\,m^{-1}\,k^{-1}}$) should be assigned an appropriate value. In this study, we employed the parameterization of Anderson (1976) that describes k_{eff} as a function of snow density ρ_{s} ($\mathrm{kg\,m^{-3}}$):

$$k_{\mathrm{eff}} = 0.021 + 2.5\left(\frac{\rho_{\mathrm{s}}}{1000}\right)^2, \tag{1}$$

an equation that is widely used in polar regions (e.g., van den Broeke et al., 2005; Kuipers Munneke et al., 2009; van As, 2011; Brun et al., 2011).

The snow surface roughness length of momentum z_0 affects turbulent heat exchanges between the snow surface and the atmosphere. Brock et al. (2006) compiled published data of z_0 and demonstrated that the values were quite dependent on surface conditions and places. Considering this, we assumed following constant values for z_0 (mm):

$$z_0 = \begin{cases} 0.12 & \text{for snow before melting} \\ 1.3 & \text{for snow after melting} \end{cases}, \tag{2}$$

which was presented by Greuell and Konzelmann (1994) and they simulated the mass balance and englacial temperature at the ETH Camp, west Greenland, during the 1990 summer melting period with these values. During IOP, the surface condition at SIGMA-A was smooth. van den Broeke et al. (2009) presented time series of z_0 at sites S5

TCD
9, 495–539, 2015

(490 m a.s.l.), S6 (1020 m a.s.l.), and S9 (1520 m a.s.l.) on the K-transect in southwest Greenland during August 2003 to August 2007. The above mentioned values for z_0 (Eq. 2) fall in the range of their result at S9, where surface condition was relatively smooth. The uncertainty of the SMAP model calculated SEB caused by the choice of z_0 is investigated in Sect. 5. In the SMAP model, roughness lengths for heat and moisture are calculated following Andreas (1987) as explained by Niwano et al. (2012).

3.3 Model configuration

In the present study we calculated temporal evolution of snow physical states in the NSL (see Sect. 2.2) at the SIGMA-A site from 30 June 2012, 16:45 UTC to 14 July 2012, 12:00 UTC. To perform detailed model simulations we divided the NSL into several thin model layers. According to Dadic et al. (2008), the recommended model vertical resolution for Arctic snowpack is on the order of 10 mm, because there is a strong feedback between small-scale snow structure and snow temperature that should be simulated accurately by snowpack models. Based on this consideration, the SMAP model vertical layer thickness (see Sect. 3.1) used in this study ranged between $d_{\mathrm{min}} = 2$ mm and $d_{\mathrm{max}} = 6$ mm. Accordingly, it became necessary for the time step of the numerical integration Δt to be shortened. Thus, Δt was set to 30 s in the present study.

Input parameters used to drive the SMAP model in the present study were air pressure; air temperature and relative humidity at 3.0 m above the snow surface (Fig. 2a); wind speed at 3.0 m above the snow surface (Fig. 2b); downward shortwave, near-infrared, and longwave radiant fluxes (Fig. 2c); accumulated precipitation (Fig. 2d); the temperature of the thick bottom ice layer in the NSL (lower boundary condition); and the mass concentrations of snow impurities (Fig. 5).

The time interval for meteorological properties was selected to be 5 min, whereas daily values were used for other properties. The corrected three-hourly accumulated precipitation data were divided equally into each time interval. Regarding the measured mass concentrations of snow impurities (Fig. 5), we followed the same method

TCD
9, 495–539, 2015

used by Niwano et al. (2012), who equated the values in the top 2 cm of the model layers of the snowpack to the corresponding observed values and assigned the observed values in the 2–10 cm depth interval equally to the lower model layers. During the period when measurements of the mass concentrations of snow impurities were unavailable (dashed lines in Fig. 5), we used the values measured at the nearest point in time. The initial physical states of the snowpack in the NSL on 30 June (profiles of snow grain shape, snow temperature, snow density, volumetric water content, and geometric snow grain size) were taken from the snow pit observations conducted on 30 June 2012, 16:45 UTC (Yamaguchi et al., 2014). These observations were distributed within the model layers, and the layer thickness d was in all cases set to 5 mm in the NSL at that time. Because the SMAP model calculates shortwave albedo as a function of snow grain size and the mass concentrations of snow impurities, information regarding an optically equivalent snow grain size profile was necessary. In the present study, an optically equivalent profile was obtained by multiplying the geometric profile by a factor that produced agreement between the calculated shortwave albedo and observations on 30 June 2012, 16:45 UTC. The assigned factor was 0.88.

4 Model evaluation using the data at the SIGMA-A site

In this section we evaluate the SMAP model using the data measured at the SIGMA-A site during the IOP to adapt it to the GrIS snowpack. The following parameters were validated quantitatively: snow temperature profile, snow surface temperature, surface snow grain size, and shortwave albedo. When a measured snow temperature profile was compared against simulation results, the depth of the NSL simulated by the model was adjusted to the measured depth. The measured snow surface temperature T_{s0} was calculated from the following relationship between the observed downward and upward longwave radiant fluxes ($L^{\downarrow}$ and $L^{\uparrow}$):

$$L^{\uparrow} = \varepsilon_s \sigma T_{s0}^4 + (1 - \varepsilon_s) L^{\downarrow}, \quad (3)$$

TCD
9, 495–539, 2015

where ε_s is the emissivity of the snow surface, and σ is the Stefan–Boltzmann constant. In the present study, we assumed $\varepsilon_s = 0.98$ (Armstrong and Brun, 2008). The model performance was assessed in terms of the root mean square error (RMSE) and mean error (ME) (Table 1). In this paper ME is defined as the average difference between simulated and observed values.

4.1 Snow temperature profile

We first examined whether the SMAP model could reproduce the internal physical states of the NSL in terms of the snow temperature profile. Model performance during the IOP (Table 1) indicated that the model tended to underestimate the snow temperature profile. However, the SMAP model satisfactorily simulated the temperatures. An example profile comparison on 8 July showed that the top 40 cm of the observed snowpack was wet (Fig. 6), and the condition was reproduced by the SMAP model. Even when such observed wet snow conditions were excluded from the statistical assessment of model performance, the order of magnitude of the RMSE and ME did not change (Table 1).

4.2 Snow surface temperature

Snow surface temperature affects all energy flux components of the SEB, except for the net shortwave radiant flux. A comparison of observed and simulated snow surface temperatures during the IOP (Fig. 7) as well as the obtained MEs (Table 1) indicated that the SMAP model tended to overestimate snow surface temperature; however, the RMSE obtained in this study (0.53 °C) was an improvement compared to the previous study by Niwano et al. (2012) at Sapporo during the winters of 2007–2009 (2.45 and 2.3 °C for the winters of 2007–2008 and 2008–2009, respectively). In this case as well, scores under dry snow surface conditions were still reasonable (RMSE = 0.85 °C, and ME = 0.55 °C). These foregoing statistics are almost the same order of magnitude as

TCD
9, 495–539, 2015

the analogous statistics from previous, detailed snow modeling studies performed in polar regions (Kuipers Munneke et al., 2009, 2012; Brun et al., 2011).

4.3 Surface snow grain size

For the SMAP model, snow grain size is one of the key parameters to be simulated accurately, because the SMAP model calculates the snow albedo and solar heating profile in the snowpack using the PBSAM, to which snow grain size is an input parameter. Figure 8a depicts the simulated snow grain size profile in the NSL, and Fig. 8b compares the surface snow grain size determined from in situ manual measurements and GRS against the simulation result. Because the GRS estimates agreed well with in situ measurements, and because we could obtain more data from GRS than from in situ manual measurements, model validation was performed against GRS data in the present study. The simulated surface snow grain size sometimes decreased abruptly (Fig. 8b), although a new snowfall event was not observed during the IOP. The abrupt decrease in grain size was caused by rapid surface melting and subsequent continuous exposure of layers beneath that were simulated by the SMAP model (Fig. 8a). The order of magnitude of the simulated snow grain size was almost the same with the SMAP model and GRS, and the RMSE (0.21 mm) and ME (0.16 mm) (Table 1) were almost the same order of magnitude as the analogous errors reported by Niwano et al. (2012) for seasonal snow simulations at Sapporo, Japan, during the winters of 2007–2009 (RMSE = 0.31 and 0.15 mm, and ME = −0.04 and −0.02 mm, for the winters of 2007–2008 and 2008–2009, respectively). During 3–5 July, when we observed surface hoar with small grains of snow on the surface at the SIGMA-A site (Yamaguchi et al., 2014), discrepancies between observations and simulations stood out (Fig. 8b). The reason for this failure is that the SMAP model could not simulate surface hoar formation during this period. In the SMAP model surface hoar is created when the latent heat flux is positive and the wind speed is less than $3\,\mathrm{m\,s^{-1}}$ (Föhn, 2001); however, the simulated H_L from the night of 2 July to the morning of 5 July was continuously negative (more detailed discussion follows in Sect. 5).

TCD
9, 495–539, 2015

In the SMAP model, the latent heat flux is calculated on the assumption that the snow surface is saturated (Niwano et al., 2012), an assumption that is widely made by many physical snowpack models. However, as Box and Steffen (2001) have pointed out, this method can detect surface hoar deposition only in cases of extreme temperature inversion, and this limitation leads to underestimation of surface hoar. Because this result suggests that reconsideration of the method of calculating the latent heat flux in the SMAP model is necessary to obtain an accurate SEB, we discuss this topic further in Sect. 5.

4.4 Shortwave albedo

Now we focus on the shortwave albedo, which is another important parameter for estimating snow-atmosphere interactions as well as snow surface temperature. Figure 9 compares observed shortwave albedos with albedos simulated with the SMAP model during the IOP. The comparison shows that the SMAP model successfully reproduced the observed diurnal variations. The RMSE and ME in Table 1 support this assessment. Furthermore, the SMAP model simulated observed spikes when snow albedo rapidly increased, especially around 4 July and after 10 July. The cause of these spikes is the fact that the snow albedo is generally higher under cloudy-sky than under clear-sky conditions (Liljequist, 1956; Yamanouchi, 1983; Aoki et al., 1999). These results imply that the component of the PBSAM driven by the observed near-infrared and UV-visible fractions of the downward shortwave radiant flux, as well as the diffuse fractions calculated by the procedure described in Sect. 3.1, played an important role in improving the precision of the SMAP model simulations.

In Sect. 4.3, however, we found clear discrepancies between observed and simulated surface snow grain size, especially during 3–5 July, when simulated shortwave albedo agreed well with observations. This paradox can be explained as follows: as demonstrated by Yamanouchi (1983), the difference between the downward near-infrared radiant fluxes under clear-sky and cloudy-sky conditions is larger than the analogous difference in the downward visible radiant fluxes. The explanation is that most of the

TCD
9, 495–539, 2015

absorption of solar radiation by clouds occurs in the near-infrared region, and the difference in multiple reflection effects due to the spectral differences of surface albedo magnifies the impact of this preferential near-infrared absorption. Figure 2c depicts the observed near-infrared fraction of the downward shortwave radiant flux. Actually, the near-infrared fraction was depleted during the cloudy-sky conditions observed on 3, 4, 6, 7, and 8 July and after 10 July (Sect. 2.1). In the PBSAM, the shortwave albedo is calculated from a weighted summation of visible albedo and near-infrared albedo. The weights for these albedos are the visible and near-infrared fractions of the downward shortwave radiant flux (Aoki et al., 2011). A decrease of the near-infrared fraction therefore increases the influence of the visible albedo on the calculated shortwave albedo, and the influence of the near-infrared albedo, which is mainly affected by snow grain size (Wiscombe and Warren, 1980), decreases. The simulated shortwave albedo therefore agreed with observations, even during 3–5 July, when the SMAP model could not reproduce surface hoar and the associated small near-surface snow grain size.

5 Reconsideration of the latent het flux calculation method

As discussed in Sect. 4.3, calculation of the latent heat flux H_L based on the assumption of the SMAP model that the snow surface is saturated might lead to underestimation of surface hoar deposition. Here we refer to this method as 1LM, in accordance with Box and Steffen (2001). According to Box and Steffen (2001), employing two-level atmospheric data to calculate H_L can solve this problem, an approach we designate as the 2LM method. As noted in Sect. 2.1, the SIGMA-A AWS measured temperature, relative humidity, and wind speed at heights of 3 and 6 m above the surface. In this section we calculate the latent heat flux using the AWS data at these two heights, and we investigate whether the SMAP model can simulate surface hoar formation with small snow grain sizes by using the 2LM method.

TCD
9, 495–539, 2015

The original formulation of H_L employed by the SMAP model (1LM) is based on the bulk method and is expressed as follows (Niwano et al., 2012):

$$H_L = \frac{\rho_a L_v \kappa^2 u_1 (q_1 - q_{s0})}{\left[\ln\left(\frac{z_1}{z_0}\right) - \Psi_M\left(\frac{z_1}{L}\right)\right]\left[\ln\left(\frac{z_1}{z_Q}\right) - \Psi_H\left(\frac{z_1}{L}\right)\right]}, \quad (4)$$

where ρ_a is the density of air, L_v is the latent heat of sublimation or evaporation, κ is the von Kármán constant, u_1 is the wind speed at a measurement height z_1 (in this study, z_1 is 3 m), q_1 and q_{s0} are the specific humidity at z_1 and the snow surface, respectively, Ψ_M and Ψ_H are profile functions for momentum and heat, respectively, z_0, and z_Q are roughness lengths for momentum and moisture, respectively, and L is the Obukhov length. If we now use atmospheric data at two heights (z_1 and z_2; z_2 is 6 m in this study), the formulation of the bulk method with the 2LM model can be rewritten as follows:

$$H_L = \frac{\rho_a L_v \kappa^2 (u_2 - u_1)(q_2 - q_1)}{\left[\ln\left(\frac{z_2}{z_1}\right) - \Psi_M\left(\frac{z_2}{L}\right) + \Psi_M\left(\frac{z_1}{L}\right)\right]\left[\ln\left(\frac{z_2}{z_1}\right) - \Psi_H\left(\frac{z_2}{L}\right) + \Psi_H\left(\frac{z_1}{L}\right)\right]}, \quad (5)$$

where u_2 and q_2 are the wind speed and specific humidity at z_2, respectively. The three unknown parameters L, Ψ_M, and Ψ_H can be calculated by the same method used by Niwano et al. (2012).

Figure 10a shows the temporal changes of the 1 h averaged latent heat fluxes calculated from two-level atmospheric measurements using the 2LM (OBS_2LM) compared to the original SMAP simulation result (SMAP_1LM). The former obviously tends to be higher than the latter, and sometimes the signs of the fluxes are different. Because the SMAP_1LM uses the simulated snow surface temperature to obtain the latent heat flux, the above mentioned discrepancy can be attributed to error of simulated snow surface temperature. We therefore also investigated the latent heat flux calculated from the atmospheric data measured at only one height (3 m) above the surface as well as the

TCD
9, 495–539, 2015

observed snow surface temperature obtained with Eq. (3) (OBS_1LM in Fig. 10a). The result indicated that the latent heat flux from SMAP_1LM was almost compatible with the heat flux OBS_1LM, and the discrepancy depended mainly on the choice of the 1LM or 2LM method. This dependency is also apparent in the results of Box and Steffen (2001).

As mentioned in Sect. 3.2, we assumed constant values for z_0 (0.12 and 1.3 mm for snow before and after melting, respectively) following Greuell and Konzelmann (1994) in this study. However, as Braithwaite (1995) pointed out, the uncertainty in z_0 causes significant error in turbulent heat flux calculations. Therefore, in order to confirm results from 1LM and 2LM are significantly different, we performed numerical sensitivity tests based on OBS_1LM, where value of z_0 was perturbed between the possible maximum and minimum values. These values were determined as follows: from the compilation by Brock et al. (2006), the maximum value for z_0 of the GrIS snow surface was found to be around 10 mm, while we assumed the minimum value for z_0 of the GrIS snow surface to be around 0.01 mm based on the results by Smeets and van den Broeke (2008). Figure 10b compares latent heat flux from OBS_1LM using the default configuration of z_0 with those from above mentioned two sensitivity tests with z_0 values of 10 and 0.01 mm. In general, absolute value of the latent heat flux was increased with the condition that z_0 was set to be 10 mm (mean difference against the original OBS_1LM was $-1.4\,\mathrm{W\,m^{-2}}$), while it was reduced if z_0 was set to be 0.01 mm (mean difference against the original OBS_1LM was $3.8\,\mathrm{W\,m^{-2}}$). However, it is still obvious that characteristics of latent heat fluxes with perturbed z_0 are significantly different from the results from OBS_2LM.

We next performed another numerical simulation with the SMAP model (SMAP_2LM). In this case the latent heat flux, which was used to assess surface hoar formation and to provide a boundary condition for the governing one-dimensional diffusion equation in the SMAP model (Niwano et al., 2012), was determined directly from the OBS_2LM case. Figure 10c compares the surface snow grain size from the SMAP_2LM case with the surface snow grain size from the SMAP_1LM case and GRS.

TCD
9, 495–539, 2015

A difference between results of the SMAP_2LM and SMAP_1LM cases is apparent on 4 July (Fig. 10c), when snow grain size is lower for the SMAP_2LM case than for the SMAP_1LM case. The low grain size estimated with SMAP_2LM (< 0.4 mm) can be attributed to modeled surface hoar formation. Actually, the latent heat flux simulated with OBS_2LM on 4 July was positive (Fig. 10a), and the winds at 3 m above the surface around 4 July were calm (Fig. 2b). These conditions are suitable for modeled surface hoar formation, as explained in Sect. 4.3. We also investigated the accuracy with which SMAP_2LM simulated the snow surface temperature and shortwave albedo, which control the SEB. The RMSE for the snow surface temperature was 0.54 °C, and the shortwave albedo was 0.026. These results are almost equivalent to the results from SMAP_1LM (Table 1) and demonstrate that input of two-level atmospheric measurements into a physical snowpack model is much preferable to driving the model with one-level atmospheric measurements; the former method is much more likely to detect surface hoar.

Although SMAP_2LM succeeded in reproducing the surface hoar detected at the SIGMA-A site during the IOP, there were still obvious discrepancies with GRS results around 2–5 July (Fig. 10c). To resolve this problem, it might be necessary to consider the possibility of a new snow grain size for surface hoar, which is now calculated as a function of air temperature in the same manner as new snowfall (Niwano et al., 2012).

6 SEB during the IOP at SIGMA-A

Finally, we look into the SEB during the IOP at the SIGMA-A site to elucidate the physical conditions of both the snowpack and the atmosphere that led to the remarkable melting around 12 July, when the record near-surface melt occurred over more than 95 % of the entire surface of the GrIS (Nghiem et al., 2012). The SEB equation (Armstrong and Brun, 2008) can be written as follows:

$$S_{\mathrm{net}} + L_{\mathrm{net}} + H_{\mathrm{S}} + H_{\mathrm{L}} + H_{\mathrm{R}} + H_{\mathrm{G}} = Q_{\mathrm{net}}, \quad (6)$$

TCD
9, 495–539, 2015

where S_{net} is the net shortwave radiant flux, L_{net} is the net longwave radiant flux, H_S is the sensible heat flux, H_R is the heat flux associated with rainfall, H_G is the subsurface conductive heat flux and Q_{net} is the net energy flux at the snow surface. As already mentioned, these fluxes are defined to be positive when they are directed into the snow surface. The snow surface is heated when the flux is positive, whereas it is cooled if the flux is negative. In this study, S_{net} and L_{net} were calculated from in situ measurements. Other fluxes on the left-hand side of Eq. (6) were estimated as a function of measured snow surface temperature by using the SMAP model. However, based on the discussion in Sect. 5, only H_L was calculated by using the 2LM approach.

Figure 11 shows the temporal changes of the 1 h averaged simulated SEB during the IOP. S_{net} remained positive throughout the IOP. L_{net} was negative for much of the time prior to 9 July but was positive most of the time after 10 July. H_S was close to $0\,W\,m^{-2}$ until 9 July, but it gradually increased after 10 July and sometimes reached about $50\,W\,m^{-2}$. The other turbulent heat flux, H_L, was negative most of the time during the first half of the IOP, but it increased after 10 July as well. After 10 July there was heavy rainfall frequently, but its impact on the SEB was quite small (H_R was less than $10\,W\,m^{-2}$ most of the time, although it sometimes reached more than $15\,W\,m^{-2}$). Finally, H_G showed clear diurnal variation: it heated the surface especially during the night time, while it was almost $0\,W\,m^{-2}$ in the daytime. As a result, until 9 July the total surface energy flux, Q_{net}, clearly varied diurnally, being negative during the night and positive during the day. However, after 10 July it remained positive.

Because there was a clear contrast in the calculated SEB characteristics during the period from 30 June to 9 July ("Period-1") and the time interval 10–14 July ("Period-2"), we compared the average SEB components between Period-1 and Period-2 (Fig. 12) to characterize the SEB at the SIGMA-A site around 12 July, when continuous melting was observed. Figure 12 reveals dramatic modulations of both S_{net} and L_{net}, and changes in H_S and H_L were also remarkable. Quantitatively, there were significant positive increments in H_S (4.0 to $15.2\,W\,m^{-2}$; $+11.3\,W\,m^{-2}$), H_L (-13.2 to $17.8\,W\,m^{-2}$; $+31.0\,W\,m^{-2}$), and L_{net} (-54.9 to $2.1\,W\,m^{-2}$; $+57.1\,W\,m^{-2}$), the total positive increment

TCD
9, 495–539, 2015

being 102.5 W m^{-2}. There was a remarkable decrease only in S_{net} (83.0 to 40.7 W m^{-2}; −42.3 W m^{-2}). As a result, Q_{net} increased by 55.0 W m^{-2} (24.9 to 79.9 W m^{-2}). These values, calculated during Period-1, are almost equal to the surface fluxes from June to August averaged during the summers of 2000–2011 over the GrIS accumulation area based on the MAR regional climate model (Fettweis et al., 2011) and MODIS data presented by Box et al. (2012).

The decrease of S_{net} was due to both a reduction of downward shortwave radiant flux (352.7 to 203.9 W m^{-2}) and a slight increase in shortwave albedo from 0.775 to 0.810. The latter value is as high as the 2000–2011 summer (June to August) average albedo over the GrIS accumulation area (0.809) reported by Box et al. (2012) and the cause of increase was due mainly to the appearance of clouds (discussed in Sect. 4.4). Modulation of H_S was caused mainly by an increase of temperature, which is clearly apparent in Fig. 2a. The cause of the increase in H_L was basically the same: increases in relative humidity and air temperature. The latter reached more than 0 °C. The abrupt transition of radiative properties is understandable from the perspective of cloud radiative forcing (defined as the difference in net surface radiant fluxes under cloudy-sky and clear-sky conditions) in the polar region: at the snow surface shortwave cloud radiative forcing is negative, and longwave cloud radiative forcing is positive (Aoki and Yamanouchi, 1992). We thus conclude that the appearance of low-level clouds (Sect. 2.1) accompanied by a remarkable increase of temperature (Fig. 2a) played an important role and induced surface heating during Period-2. The heating occurred via a large increase in L_{net}, which was able to substantially compensate for the reduction of S_{net}. Bennartz et al. (2013) have investigated the effect of clouds on the temporal development of surface temperature by performing numerical sensitivity tests with a prognostic surface energy balance model and by parameterizing downward radiant fluxes at the surface. They have argued that low-level, liquid clouds played a critical role in the enhancement of surface melting at Summit, Greenland by increasing near-surface temperature through their radiative effects. The present results, which highlight the importance of low-level clouds, are consistent with their conclusion.

TCD
9, 495–539, 2015

7 Conclusions

In this study, we investigated the record near-surface melt event that occurred over the GrIS during the IOP (30 June to 14 July 2012) from the standpoint of the SEB. We used data measured in situ at the SIGMA-A site, where significant increases of air temperature, relative humidity, and downward longwave radiant flux, as well as heavy rainfall and abrupt near-surface snowmelt, were observed beginning on 10 July. Although radiation-related components of the SEB could be determined from AWS data, other fluxes were not measured directly. We therefore employed the physical snowpack model SMAP to calculate the H_S, H_L, and H_R. Because this was the first attempt to adapt the SMAP model to a polar region, we carried out a preliminary analysis of various aspects of the performance of the SMAP model. We calculated the snow temperature profile in the NSL, snow surface temperature, surface snow grain size, and shortwave albedo; we compared these calculated values with in situ measurements. In the numerical simulation, the initial conditions of the snow were specified from the snow pit measurements conducted on 30 June 2012, 16:45 UTC. The SMAP model was subsequently driven by 5 min averaged meteorological data, including air pressure; air temperature; relative humidity; wind speed; and downward shortwave, near-infrared, and longwave radiant fluxes. The SMAP model was also driven by the daily temperature at the bottom of the thick ice layer in the NSL, the mass concentrations of snow impurities obtained every other day, and 5 min averaged accumulated precipitation based on 3 hourly ERA-Interim reanalysis data corrected by in situ bucket measurements.

Validation results revealed that the RMSE for the snow temperature profile and snow surface temperature were comparable and reasonable. Regarding surface snow grain size, simulation results were compared against GRS data obtained from spectral albedo measurements post-processed with a GSAF algorithm. Although the RMSE and ME that we obtained were comparable in magnitude to those reported from previous model validation studies performed at Sapporo, Japan, the small snow grain size

TCD
9, 495–539, 2015

associated with the surface hoar observed during 3–5 July could not be simulated by the SMAP model. In the SMAP model, surface hoar is created when H_L is positive and the wind speed is less than $3\,m\,s^{-1}$. However, the simulated H_L from the night of 2 July to the morning of 5 July was continuously negative. Despite these discrepancies, the simulated shortwave albedo was in reasonable agreement with observations throughout the IOP (RMSE = 0.023, and ME = 0.008). The cause of the agreement between the simulated shortwave albedo and observations, even during the 3–5 July period when the SMAP model could not reproduce surface hoar and associated small near-surface snow grain size, was a decrease of the near-infrared fraction of the downward shortwave radiant flux caused by the appearance of low-level clouds during the IOP. This change in the shortwave radiant flux increased the influence of visible albedo and in turn decreased the effect of near-infrared albedo on the shortwave albedo.

Because the method of calculating the H_L needed to be improved to obtain an accurate SEB in the validation of the snow grain size calculated with the SMAP model, we performed another numerical simulation with the SMAP model. In this simulation, 2-level data for air temperature, relative humidity, and wind speed were used to calculate H_L with the 2LM method, which calculated H_L from atmospheric profiles only and did not require the condition originally assumed by the SMAP model that the snow surface was saturated (1LM). In this case, the calculated H_L around 4 July turned positive, and the SMAP model was able to detect surface hoar deposition as well as simulate the associated small surface snow grain size. Because results from 1LM are affected by the choice of z_0, we performed numerical sensitivity tests, where values of z_0 were perturbed between the possible maximum and minimum values (10 and 0.01 mm, respectively). As a result, we confirmed that characteristics of latent heat flux from 1LM is significantly different from that from 2LM. Based on these results, we could confirm that the 2LM method was an effective way to obtain an accurate H_L. Although it is presently quite common to run land surface models by forcing with 1-level meteorological data, the present results suggest that it is preferable to input 2-level atmospheric measurements (if available) into a physical snowpack model, because this method increases the

TCD
9, 495–539, 2015

likelihood of detecting surface hoar compared to the probability if 1-level atmospheric measurements are employed to drive the model.

Finally, we investigated the SEB at the SIGMA-A site during the IOP. Radiation-related components of the SEB were directly given from the AWS measurements, whereas other components, except for H_L, were calculated by the SMAP model as a function of measured snow surface temperature. The H_L was calculated with the 2LM method based on the results mentioned above. The calculated SEB was clearly different between Period-1 (30 June to 9 July) and Period-2 (10 to 14 July): L_{net} increased dramatically by $+57.1\,W\,m^{-2}$ (H_S and H_L also increased by +11.3 and $+31.0\,W\,m^{-2}$, respectively) after 10 July, whereas S_{net} decreased significantly by $-42.3\,W\,m^{-2}$. Consequently, Q_{net} clearly varied diurnally (negative during the night and positive during the day) until 9 July. However, the fact that it remained continuously positive after 10 July explains the continuous melt event observed at the SIGMA-A site. We discussed the reason for this remarkable transition of radiative properties, and we concluded that it was caused by the appearance of low-level clouds accompanied by a significant temperature increase. The result was surface heating during Period-2 via the process of cloud radiative forcing in the polar region.

Author contributions. M. Niwano developed the SMAP model code and performed the numerical calculations. T Aoki designed the SIGMA AWS system. T. Aoki, S. Matoba, S. Yamaguchi, T. Tanikawa, M. Niwano, K. Kuchiki, and H. Motoyama installed the SIGMA-A AWS on the GrIS and constructed data-acquisition system. S. Matoba and S. Yamaguchi performed snow pit measurements. T. Aoki and K. Kuchiki processed data of mass concentrations of snow impurities. M. Niwano, T. Aoki, and T. Tanikawa conducted spectral albedo measurements. K. Kuchiki retrieved GRS from the spectral albedo data. M. Niwano prepared the manuscript with contributions from all co-authors.

Acknowledgements. We sincerely thank Tetsuhide Yamasaki for logistical and field support of our expedition, and Sakiko Daorana for her help during our stay at Qaanaaq, Greenland. We thank Climatec Inc. (Japan) for manufacturing the AWS installed at the SIGMA-A site, and Masae Igosaki for supporting the laboratory measurements of snow impurities. This study was supported in part by (1) the Japan Society for the Promotion of Science (JSPS), Grant-in-Aid for

TCD
9, 495–539, 2015

Scientific Research (S), number 23221004, (2) the Global Change Observation Mission – Climate (GCOM-C)/the Second-generation GLobal Imager (SGLI) Mission, the Japan Aerospace Exploration Agency (JAXA), (3) the Experimental Research Fund for Global Environment Conservation, the Ministry of the Environment of Japan, and (4) the Grant for Joint Research Program, the Institute of Low Temperature Science, Hokkaido University. The map showing the location of site SIGMA- A (Fig. 1) was created by NunaGIS (http://en.nunagis.gl/) operated by Asiaq, Greenland Survey.

References

Anderson, E. A.: A point energy and mass balance model of a snow cover, NOAA Tech. Rep. NWS19, Office of Hydrology, National Weather Service, Silver Spring, Maryland, US, 1976.

Andreas, E. L.: A theory for the scalar roughness and the scalar transfer coefficients over snow and ice, Bound.-Lay- Meteorol., 38, 159–184, doi:10.1007/BF00121562, 1987.

Aoki, T. and Yamanouchi, T.: Cloud radiative forcing around Asuka Station, Antarctica, Proc. NIPR Symp. Polar Meteorol. Glaciol., 5, 76–89, 12–13 July 1990, Tokyo, 1992.

Aoki, T., Aoki, T., Fukabori, M., and Uchiyama, A.: Numerical simulation of the atmospheric effects on snow albedo with multiple scattering radiative transfer model for the atmosphere-snow system, J. Meteorol. Soc. Jpn., 77, 595–614, 1999.

Aoki, T., Aoki, T., Fukabori, M., Hachikubo, A., Tachibana, Y., and Nishio, F.: Effects of snow physical parameters on spectral albedo and bidirectional reflectance of snow surface, J. Geophys. Res., 105, 10219–10236, doi:10.1029/1999JD901122, 2000.

Aoki, T., Hachikubo, A., and Hori, M.: Effects of snow physical parameters on shortwave broadband albedos, J. Geophys. Res., 108, 4616, doi:10.1029/2003JD003506, 2003.

Aoki, T., Hori, M., Motoyoshi, H., Tanikawa, T., Hachikubo, A., Sugiura, K., Yasunari, T. J., Storvold, R., Eide, H. A., Stamnes, K., Li, W., Nieke, J., Nakajima, Y., and Takahashi, F.: ADEOS-II/GLI snow/ice products – Part II: Validation results using GLI and MODIS data, Remote Sens. Environ., 111, 274–290, doi:10.1016/j.rse.2007.02.035, 2007.

Aoki, T., Kuchiki, K., Niwano, M., Kodama, Y., Hosaka, M., and Tanaka, T.: Physically based snow albedo model for calculating broadband albedos and the solar heating profile in snowpack for general circulation models, J. Geophys. Res., 116, D11114, doi:10.1029/2010JD015507, 2011.

TCD
9, 495–539, 2015

Aoki, T., Matoba, S., Uetake, J., Takeuchi, N., and Motoyama, H.: Field activities of the "Snow Impurity and Glacial Microbe effects on abrupt warming in the Arctic" (SIGMA) project in Greenland in 2011–2013, Bull. Glaciol. Res., 32, 3–20, doi:10.5331/bgr.32.3, 2014a.

Aoki, T., Matoba, S., Yamaguchi, S., Tanikawa, T., Niwano, M., Kuchiki, K., Adachi, K., Uetake, J., Motoyama, H., and Hori, M.: Light-absorbing snow impurity concentrations measured on Northwest Greenland ice sheet in 2011 and 2012, Bull. Glaciol. Res., 32, 21–31, doi:10.5331/bgr.32.21, 2014b.

Armstrong, R. L. and Brun, E. (Eds.): Snow and Climate: Physical Processes, Surface Energy Exchange and Modeling, Cambridge Univ. Press, Cambridge, UK, 2008.

Bennartz, R., Shupe, M. D., Turner, D. D., Walden, V. P., Steffen, K., Cox, C. J., Kulie, M. S., Miller, N. B., and Pettersen, C.: July 2012 Greenland melt extent enhanced by low-level liquid clouds, Nature, 496, 83–86, doi:10.1038/nature12002, 2013.

Box, J. E. and Steffen, K.: Sublimation on the Greenland ice sheet from automated weather station observations, J. Geophys. Res., 106, 33965–33981, doi:10.1029/2001JD900219, 2001.

Box, J. E., Fettweis, X., Stroeve, J. C., Tedesco, M., Hall, D. K., and Steffen, K.: Greenland ice sheet albedo feedback: thermodynamics and atmospheric drivers, The Cryosphere, 6, 821–839, doi:10.5194/tc-6-821-2012, 2012.

Braithwaite, R. J.: Aerodynamic stability and turbulent sensible-heat flux over a melting ice surface, the Greenland ice sheet, J. Glaciol., 41, 562–571, 1995.

Brock, B. W., Willis, I. C., and Sharp, M. J.: Measurement and parameterization of aerodynamic roughness length variations at Haut Glacier d'Arolla, Switzerland, J. Glaciol., 52, 281–297, 2006.

Brun, E., Martin, E., Simon, V., Gendre, C., and Coleou, C.: An energy and mass model of snow cover suitable for operational avalanche forecasting, J. Glaciol., 35, 333–342, 1989.

Brun, E., David, P., Sudul, M., and Brunot, G.: A numerical model to simulate snow-cover stratigraphy for operational avalanche forecasting, J. Glaciol., 38, 13–22, 1992.

Brun, E., Six, D., Picard, G., Vionnet, V., Arnaud, L., Bazile, E., Boone, A., Bouchard, A., Genthon, C., Guidard, V., Le Moigne, P., Rabier, F., and Seity, Y.: Snow/atmosphere coupled simulation at Dome C, Antarctica, J. Glaciol., 52, 721–736, doi:10.3189/002214311797409794, 2011.

Carmagnola, C. M., Morin, S., Lafaysse, M., Domine, F., Lesaffre, B., Lejeune, Y., Picard, G., and Arnaud, L.: Implementation and evaluation of prognostic representations of the optical

TCD
9, 495–539, 2015

diameter of snow in the SURFEX/ISBA-Crocus detailed snowpack model, The Cryosphere, 8, 417–437, doi:10.5194/tc-8-417-2014, 2014.

Dadic, R., Schneebeli, M., Lehning, M., Hutterli, M. A., and Ohmura, A.: Impact of the microstructure of snow on its temperature: a model validation with measurements from Summit, Greenland, J. Geophys. Res., 113, D14303, doi:10.1029/2007JD009562, 2008.

Dee, D. P., Uppala, S. M., Simmons, A. J., Berrisford, P., Poli, P., Kobayashi, S., Andrae, U., Balmaseda, M. A., Balsamo, G., Bauer, P., Bechtold, P., Beljaars, A. C. M., van de Berg, L., Bidlot, J., Bormann, N., Delsol, C., Dragani, R., Fuentes, M., Geer, A. J., Haimberger, L., Healy, S. B., Hersbach, H., Hólm, E. V., Isaksen, L., Kållberg, P., Köhler, M., Matricardi, M., McNally, A. P., Monge-Sanz, B. M., Morcrette, J.-J., Park, B.-K., Peubey, C., de Rosnay, P., Tavolato, C., Thépaut, J.-N., and Vitart, F.: The ERA-Interim reanalysis: configuration and performance of the data assimilation system, Q. J. Roy. Meteor. Soc., 137, 553–597, doi:10.1002/qj.828, 2011.

Fettweis, X., Tedesco, M., van den Broeke, M., and Ettema, J.: Melting trends over the Greenland ice sheet (1958–2009) from spaceborne microwave data and regional climate models, The Cryosphere, 5, 359–375, doi:10.5194/tc-5-359-2011, 2011.

Fettweis, X., Hanna, E., Lang, C., Belleflamme, A., Erpicum, M., and Gallée, H.: *Brief communication* "Important role of the mid-tropospheric atmospheric circulation in the recent surface melt increase over the Greenland ice sheet", The Cryosphere, 7, 241–248, doi:10.5194/tc-7-241-2013, 2013.

Fierz, C., Armstrong, R. L., Durand, Y., Etchevers, P., Greene, E., McClung, D. M., Nishimura, K., Satyawali, P. K., and Sokratov, S. A.: The International Classification for Seasonal Snow on the Ground, IHP-VII Technical Documents in Hydrology N_83, IACS Contribution N_1, UNESCO-IHP, Paris, viii, 80 pp., 2009.

Föhn, P. M. B.: Simulation of surface-hoar layers for snow-cover models, Ann. Glaciol., 32, 19–26, doi:10.3189/172756401781819490, 2001.

Goudriaan, J.: Crop Micrometeorology: A Simulation Study, Pudoc, Wageningen, Netherlands, 1977.

Greuell, W. and Konzelmann, T.: Numerical modelling of the energy balance and the englacial temperature of the Greenland Ice Sheet. Calculations for the ETH-Camp location (West Greenland, 1155 m a.s.l.), Global Planet. Change, 9, 91–114, doi:10.1016/0921-8181(94)90010-8, 1994.

TCD
9, 495–539, 2015

Hall, D. K., Comiso, J. C., DiGirolamo, N. E., Shuman, C. A., Box, J. E., and Koenig, L. S.: Variability in the surface temperature and melt extent of the Greenland ice sheet from MODIS, Geophys. Res. Lett., 40, 2114–2120, doi:10.1002/grl.50240, 2013.

Hanna, E., Fettweis, X., Mernild, S. H., Cappelen, J., Ribergaard, M. H., Shuman, C. A., Steffen, K., Wood, L., and Mote, T. L.: Atmospheric and oceanic climate forcing of the exceptional Greenland ice sheet surface melt in summer 2012, Int. J. Climatol., 34, 1022–1037, doi:10.1002/joc.3743, 2014.

Hirashima, H., Yamaguchi, S., Sato, A., and Lehning, M.: Numerical modeling of liquid water movement through layered snow based on new measurements of the water retention curve, Cold Reg. Sci. Technol., 64, 94–103, doi:10.1016/j.coldregions.2010.09.003, 2010.

Ishimoto, H., Masuda, K., Mano, Y., Orikasa, N., and Uchiyama, A.: Irregularly shaped ice aggregates in optical modeling of convectively generated ice clouds, J. Quant. Spectrosc. Ra., 113, 632–643, doi:10.1016/j.jqsrt.2012.01.017, 2012.

Khan, S. A., Wahr, J., Bevis, M., Velicogna, I., and Kendrick, E.: Spread of ice mass loss into northwest Greenland observed by GRACE and GPS, Geophys. Res. Lett., 37, L06501, doi:10.1029/2010GL042460, 2010.

Kuchiki, K., Aoki, T., Tanikawa, T., and Kodama, Y.: Retrieval of snow physical parameters using a ground-based spectral radiometer, Appl. Optics, 48, 5567–5582, doi:10.1364/AO.48.005567, 2009.

Kuipers Munneke, P., van den Broeke, M. R., Reijmer, C. H., Helsen, M. M., Boot, W., Schneebeli, M., and Steffen, K.: The role of radiation penetration in the energy budget of the snowpack at Summit, Greenland, The Cryosphere, 3, 155–165, doi:10.5194/tc-3-155-2009, 2009.

Kuipers Munneke, P., van den Broeke, M. R., King, J. C., Gray, T., and Reijmer, C. H.: Near-surface climate and surface energy budget of Larsen C ice shelf, Antarctic Peninsula, The Cryosphere, 6, 353–363, doi:10.5194/tc-6-353-2012, 2012.

Lehning, M., Bartelt, P., Brown, B., Fierz, C., and Satyawali, P.: A physical SNOWPACK model for the Swiss avalanche warning. Part II: Snow microstructure, Cold Reg. Sci. Technol., 35, 147–167, doi:10.1016/S0165-232X(02)00073-3, 2002.

Liljequist, G. H.: Energy Exchanges of an Antarctic Snow-Field: Short-Wave Radiation, Norwegian-British-Swedish Antarctic Expedition (Maudheim, 71°03′ S, 10°56′ W), 1949–52, Scientific Results, Vol. 2, Part 1A, Norsk Polarinstitutt, Oslo, 107 pp., 1956.

TCD
9, 495–539, 2015

Nghiem, S. V., Hall, D. K., Mote, T. L., Tedesco, M., Albert, M. R., Keegan, K., Shuman, C. A., DiGirolamo, N. E., and Neumann, G.: The extreme melt across the Greenland ice sheet in 2012, Geophys. Res. Lett., 39, L20502, doi:10.1029/2012GL053611, 2012.

Niwano, M., Aoki, T., Kuchiki, K., Hosaka, M., and Kodama, Y.: Snow Metamorphism and Albedo Process (SMAP) model for climate studies: model validation using meteorological and snow impurity data measured at Sapporo, Japan, J. Geophys. Res., 117, F03008, doi:10.1029/2011JF002239, 2012.

Niwano, M., Aoki, T., Kuchiki, K., Hosaka, M., Kodama, Y., Yamaguchi, S., Motoyoshi, H., and Iwata, Y.: Evaluation of updated physical snowpack model SMAP, Bull. Glaciol. Res., 32, 65–78, doi:10.5331/bgr.32.65, 2014.

Pinzer, B. R. and Schneebeli, M.: Snow metamorphism under alternating temperature gradients: morphology and recrystallization in surface snow, Geophys. Res. Lett., 36, L23503, doi:10.1029/2009GL039618, 2009.

Richards, L. A.: Capillary conduction of liquids through porous mediums, J. Appl. Phys., 1, 318–333, doi:10.1063/1.1745010, 1931.

Shimizu, H.: Air Permeability of Deposited Snow, Contributions from the Institute of Low Temperature Science, A22, 1–32, Institute of Low Temperature Science, Hokkaido University, Sapporo, Japan, 1970.

Smeets, C. J. P. P. and van den Broeke, M. R.: Temporal and spatial variations of the aerodynamic roughness length in the ablation zone of the Greenland ice sheet, Bound.-Lay. Meteorol., 128, 315–338, doi:10.1007/s10546-008-9291-0, 2008.

Tedesco, M., Fettweis, X., Mote, T., Wahr, J., Alexander, P., Box, J. E., and Wouters, B.: Evidence and analysis of 2012 Greenland records from spaceborne observations, a regional climate model and reanalysis data, The Cryosphere, 7, 615–630, doi:10.5194/tc-7-615-2013, 2013.

van As, D.: Warming, glacier melt and surface energy budget from weather station observations in the Melville Bay region of northwest Greenland, J. Glaciol., 57, 208–220, doi:10.3189/002214311796405898, 2011.

van den Broeke, M., Reijmer, C., and van de Wal, R.: Surface radiation balance in Antarctica as measured with automatic weather stations, J. Geophys. Res., 109, D09103, doi:10.1029/2003JD004394, 2004.

TCD
9, 495–539, 2015

van den Broeke, M., Reijmer, C., van As, D., van de Wal, R., and Oerlemans, J.: Seasonal cycles of Antarctic surface energy balance from automatic weather stations, Ann. Glaciol., 41, 131–139, 2005.
van den Broeke, M., Reijmer, C., van As, D., and Boot, W.: Daily cycle of the surface energy balance in Antarctica and the influence of clouds, Int. J. Climatol., 26, 1587–1605, doi:10.1002/joc.1323, 2006.
van den Broeke, Smeets, P., and Ettema, J.: Surface layer climate and turbulent exchange in the ablation zone of the west Greenland ice sheet, Int. J. Climatol., 29, 2309–2323, doi:10.1002/joc.1815, 2009.
van Genuchten, M. T.: A closed-form equation for predicting the hydraulic conductivity of unsaturated soil, Soil Sci. Soc. Am. J., 44, 892–898, 1980.
Vionnet, V., Brun, E., Morin, S., Boone, A., Faroux, S., Le Moigne, P., Martin, E., and Willemet, J.-M.: The detailed snowpack scheme Crocus and its implementation in SURFEX v7.2, Geosci. Model Dev., 5, 773–791, doi:10.5194/gmd-5-773-2012, 2012.
Wiscombe, W. J. and Warren, S. G.: A model for the spectral albedo of snow. I: Pure snow, J. Atmos. Sci., 37, 2712–2733, doi:10.1175/1520-0469(1980)037<2712:AMFTSA>2.0.CO;2, 1980.
Yamaguchi, S., Katsushima, T., Sato, A., and Kumakura, T.: Water retention curve of snow with different grain sizes, Cold Reg. Sci. Technol., 64, 87–93, doi:10.1016/j.coldregions.2010.05.008, 2010.
Yamaguchi, S., Watanabe, K., Katsushima, T., Sato, A., and Kumakura, T.: Dependence of the water retention curve of snow on snow characteristics, Ann. Glaciol., 53, 6–12, doi:10.3189/2012AoG61A001, 2012.
Yamaguchi, S., Matoba, S., Yamazaki, T., Tsushima, A., Niwano, M., Tanikawa, T., and Aoki, T.: Glaciological observations in 2012 and 2013 at SIGMA-A site, Northwest Greenland, Bull. Glaciol. Res., 32, 95–105, doi:10.5331/bgr.32.95, 2014.
Yamanouchi, T.: Variations of incident solar flux and snow albedo on the solar zenith angle and cloud cover, at Mizuho station, Antarctica, J. Meteorol. Soc. Jpn., 61, 879–893, 1983.
Yukimoto, S., Yoshimura, H., Hosaka, M., Sakami, T., Tsujino, H., Hirabara, M., Tanaka, T. Y., Deushi, M., Obata, A., Nakano, H., Adachi, Y., Shindo, E., Yabu, S., Ose, T., and Kitoh, A.: Meteorological Research Institute Earth System Model Version 1 (MRI-ESM1) – Model Description, Tech. Rep. of MRI, 64, 83 pp., available at: http://www.mri-jma.go.jp/Publish/Technical/index_en.html, 2011.

TCD
9, 495–539, 2015

Table 1. Comparison of SMAP simulation results with in situ measurements. RMSE and ME are the root mean square error and mean error (the average of the difference between simulated values and observed values), respectively. Figures in parentheses indicate scores when the observed temperature was negative (i.e., dry snow conditions).

Parameters	RMSE	ME
Snow temperature profile (°C)	0.59 (0.80)	−0.16 (−0.23)
Snow surface temperature (°C)	0.53 (0.85)	0.21 (0.55)
Surface snow grain size (mm)	0.21	0.16
Shortwave albedo	0.023	0.008

TCD
9, 495–539, 2015

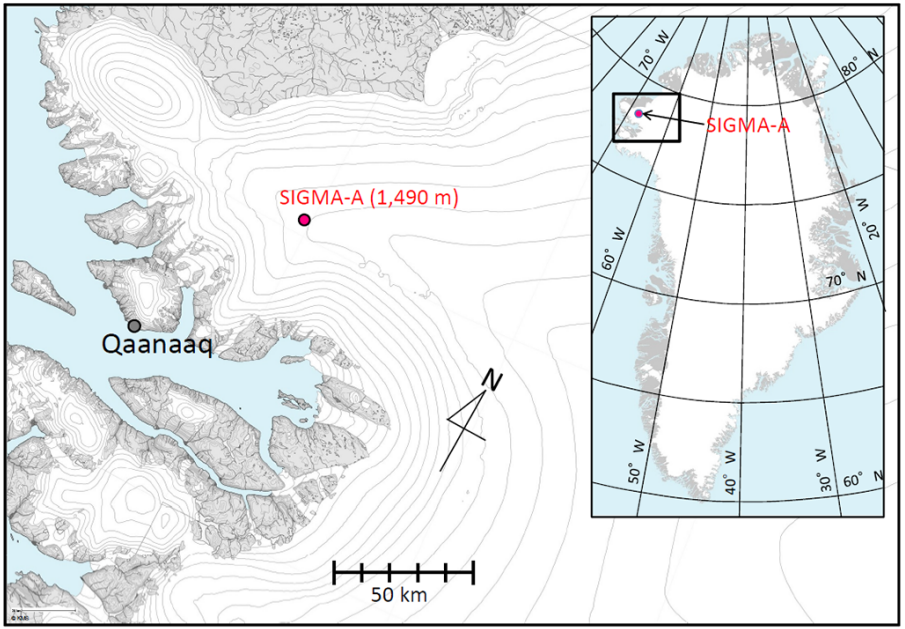

Figure 1. The location of site SIGMA-A together with ice sheet surface elevation contours (m a.s.l.). Height interval is 100 m.

TCD
9, 495–539, 2015

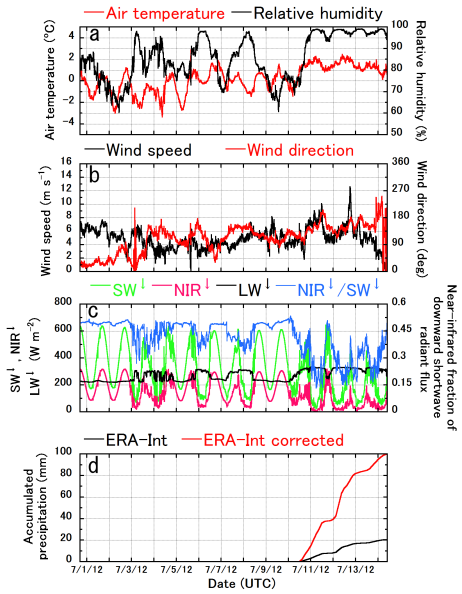

Figure 2. Meteorological conditions measured at SIGMA-A during the IOP: **(a)** air temperature and relative humidity observed at 3.0 m above the snow surface on 29 June 2012; **(b)** wind speed and direction observed at 3.0 m above the snow surface on 29 June 2012 (Wind direction is denoted in degrees that indicate the direction from which the wind is blowing. The degrees increase from 0 to 360 as the direction is rotated clockwise from north.); **(c)** downward shortwave ($SW^{\downarrow}$), near-infrared ($NIR^{\downarrow}$), longwave ($LW^{\downarrow}$) radiant fluxes, and the near-infrared fraction of the $SW^{\downarrow}$; and **(d)** accumulated precipitation obtained from 3 hourly ERA-Interim reanalysis data (ERA-Int), where the black line denotes the original amount of precipitation and the red line reflects the correction based on in situ measurements of accumulated precipitation measured during the period from 20:00 UTC on 12 July 2012 to 11:00 UTC on 14 July 2012.

TCD
9, 495–539, 2015

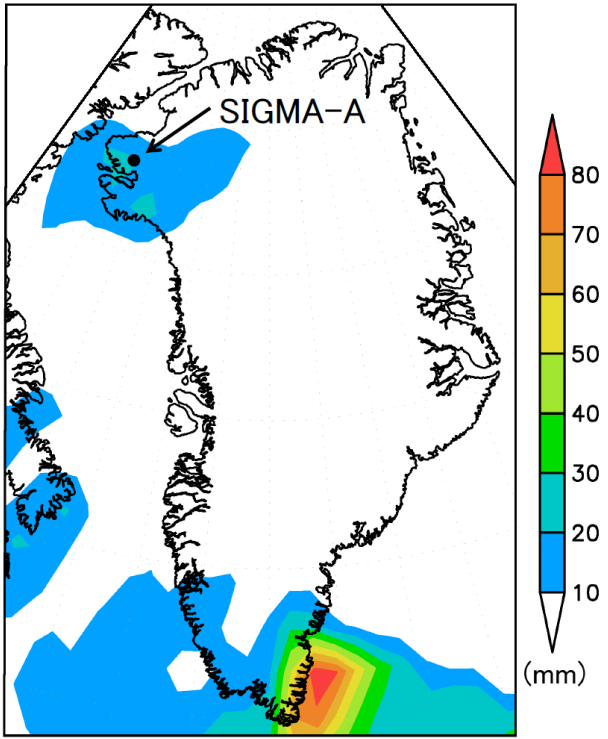

Figure 3. Accumulated precipitation from 00:00 UTC on 10 July 2012 to 12:00 UTC on 14 July 2012 obtained from the 3 hourly ERA-Interim reanalysis data. Black colored circle indicates the location of site SIGMA-A.

TCD
9, 495–539, 2015

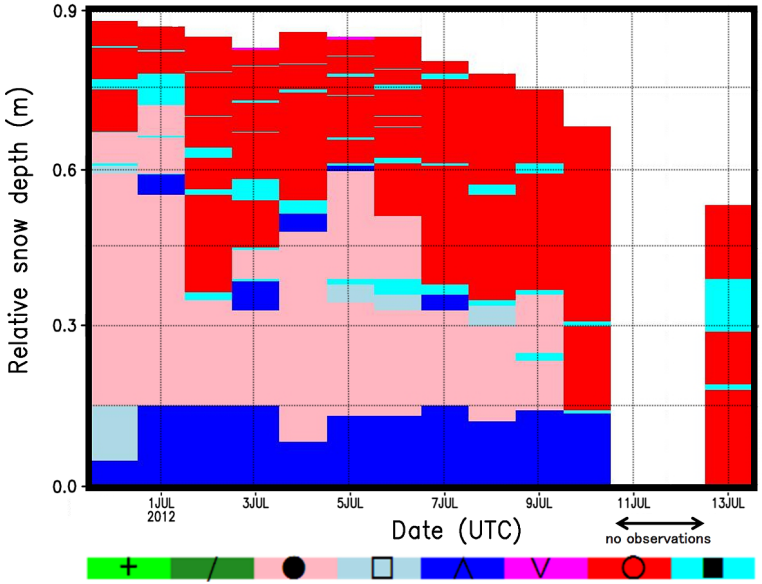

Figure 4. Temporal evolution of observed main snow grain shape profile within the NSL, which was defined by a thick bottom ice layer, at SIGMA-A during the IOP. Vertical axis (relative snow depth) denotes the height above the bottom thick ice layer. Characters and colors indicating snow grain shape follow the definition by Fierz et al. (2009). In sequence from the left they denote precipitation particles, decomposing and fragmented precipitation particles, rounded grains, faceted crystals, depth hoar, surface hoar, melt forms, and ice layer.

TCD
9, 495–539, 2015

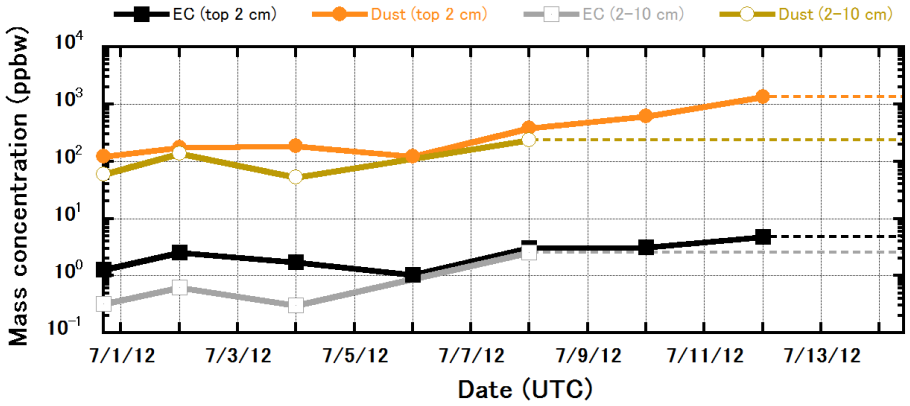

Figure 5. Measured mass concentrations of elemental carbon (EC) and dust in the top 2 cm of snow layers and the subsurface (2–10 cm) layers at the SIGMA-A site during the IOP. Dashed lines indicate periods when there were no measurements.

TCD
9, 495–539, 2015

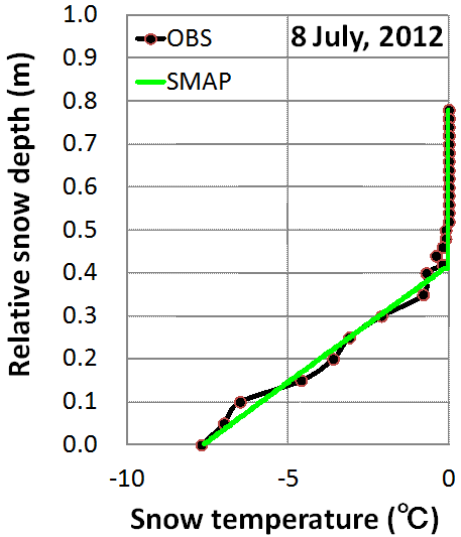

Figure 6. Comparison of snow temperature profiles in the NSL at the SIGMA-A site between snow pit observations (OBS) and profiles simulated with the SMAP model at 11:30 UTC on 8 July 2012. Relative snow depth denotes the height of the NSL above the thick bottom layer of ice. The snow depths simulated by the SMAP model were adjusted to the measurements.

TCD
9, 495–539, 2015

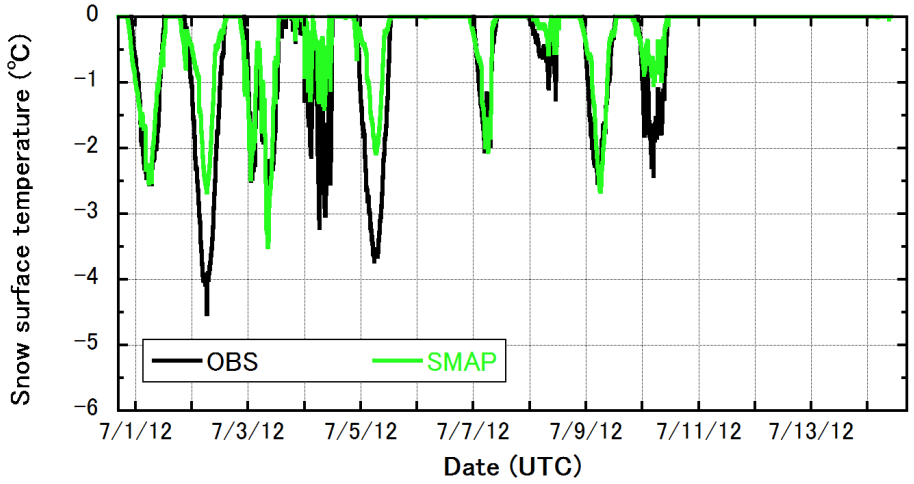

Figure 7. Snow surface temperature at the SIGMA-A site during the IOP observed with the AWS and simulated by the SMAP model. Observed snow surface temperature was calculated from observed downward and upward longwave radiant fluxes (Sect. 4).

TCD
9, 495–539, 2015

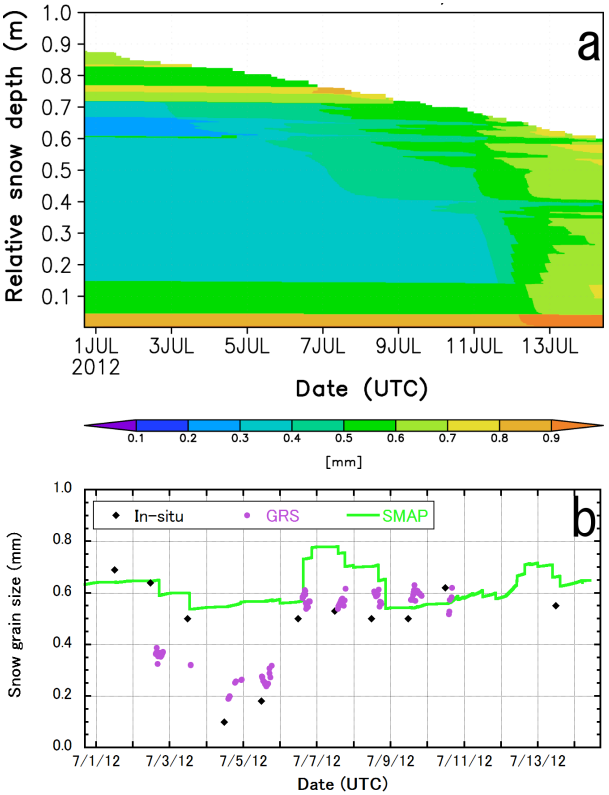

Figure 8. Temporal evolution of **(a)** simulated snow grain size profile in the NSL, and **(b)** surface snow grain size from in situ snow pit observations (black diamond patterns), ground-based remote sensing (GRS) using spectral albedo data measured with a spectrometer (purple dots), and simulated by the SMAP model (solid green curve) at the SIGMA-A site during the IOP. Vertical axis in the upper panel (relative snow depth) denotes the height above the thick bottom ice layer in the NSL.

TCD
9, 495–539, 2015

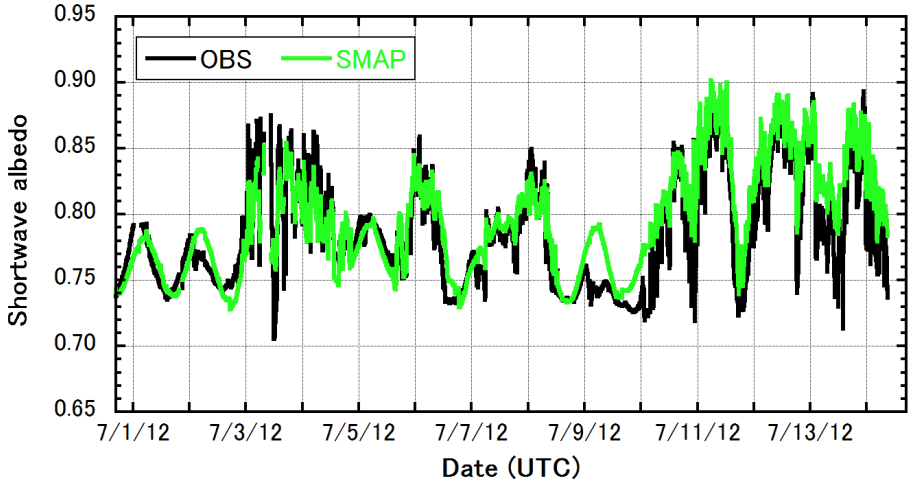

Figure 9. Shortwave albedos at the SIGMA-A site during the IOP observed with AWS and simulated by the SMAP model.

TCD
9, 495–539, 2015

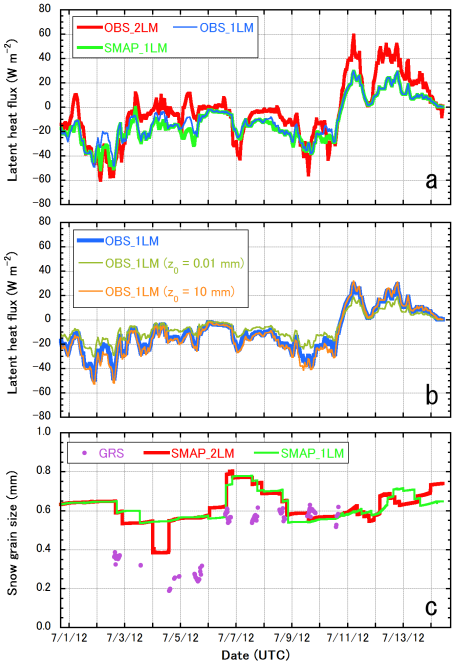

Figure 10. (a) Temporal evolution of 1 h averaged latent heat fluxes calculated from atmospheric measurements at 6 and 3 m above the surface (OBS_2LM) and measurements at 3 m above the surface (OBS_1LM), as well as the SMAP simulation forced by 1-level (3 m above the surface) atmospheric measurements (SMAP_1LM). **(b)** Comparison of 1 h averaged latent heat flux from OBS_1LM with those from two sensitivity tests, where z_0 are changed to be 0.01 and 10 mm from default OBS_1LM setting. **(c)** Comparison of surface snow grain size at the SIGMA-A site during the IOP with surface snow grain size from ground-based remote sensing (GRS) using spectral albedo data measured with a spectrometer and those from the SMAP simulations driven by 2-level (6 and 3 m above the surface) atmospheric measurements (SMAP_2LM) or 1-level (3 m above the surface) atmospheric measurements (SMAP_1LM).

TCD
9, 495–539, 2015

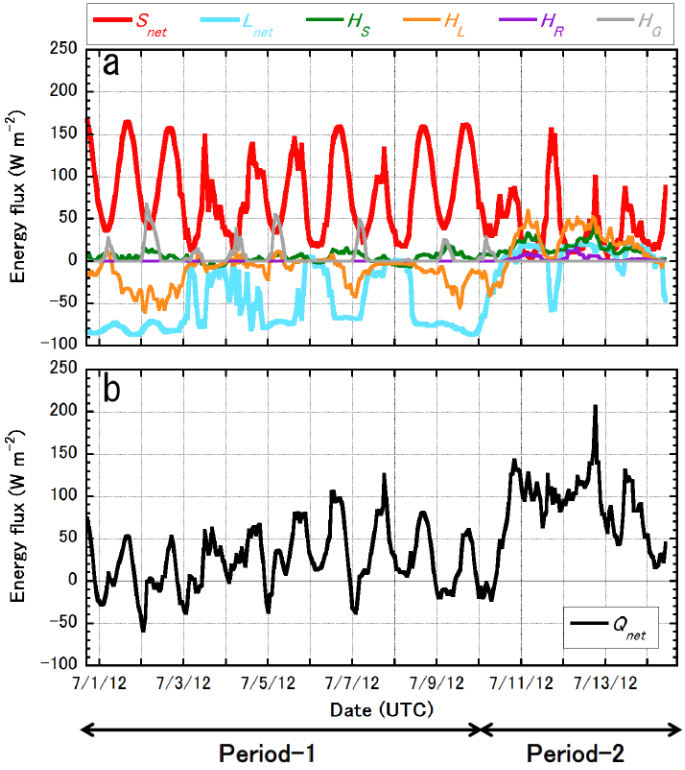

Figure 11. One-hour averaged surface energy balance at the SIGMA-A site during the IOP. The upper panel **(a)** shows net shortwave radiant flux (S_{net}), net longwave radiant flux (L_{net}), sensible heat flux (H_S), latent heat flux (H_L), heat supply by rainfall (H_R), and subsurface conductive heat flux (H_G). These fluxes are defined to be positive when they are directed into the snow surface. The lower panel **(b)** denotes net energy flux (Q_{net}). The snow surface is heated when Q_{net} is positive, whereas it is cooled if Q_{net} is negative.

TCD
9, 495–539, 2015

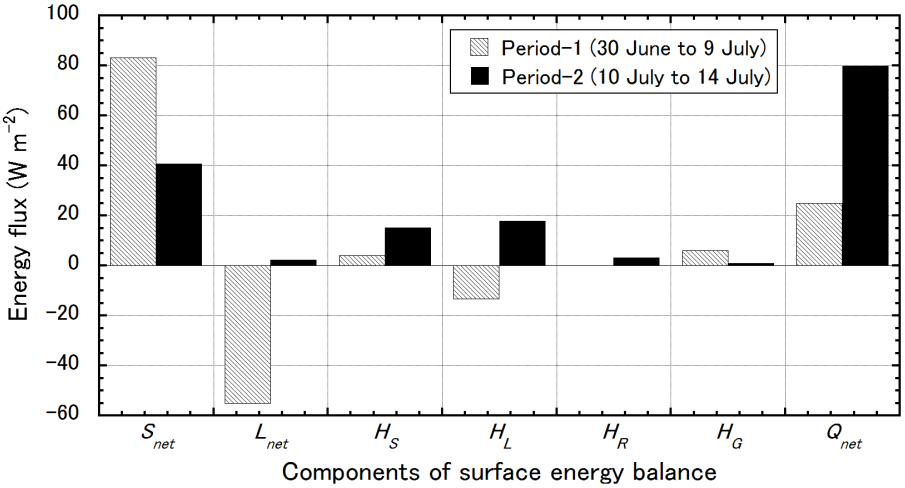

Figure 12. Comparison of average surface energy balance components (S_{net}: net shortwave radiant flux, L_{net}: net longwave radiant flux, H_S: sensible heat flux, H_L: latent heat flux, H_R: heat supply by rainfall, H_G: subsurface conductive heat flux, and Q_{net}: net energy flux) between Period-1 and Period-2 at the SIGMA-A site.

TCD
9, 495–539, 2015